

## Water-window x-ray emission from laser-produced Au plasma under optimal target thickness and focus conditions

Jiahao Wang <sup>1</sup>, Maki Kishimoto,<sup>1</sup> Tomoyuki Jozaki <sup>1,2</sup>, Tomohiro Kumeda,<sup>1</sup> Takeshi Higashiguchi <sup>3</sup>,  
Atsushi Sunahara <sup>2,4</sup>, Hikari Ohiro,<sup>1</sup> Kotaro Yamasaki <sup>1</sup> and Shinichi Namba <sup>1,\*</sup>

<sup>1</sup>Department of Advanced Science and Engineering, Hiroshima University, 1-4-1 Kagamiyama,  
Higashihiroshima 739-8527, Hiroshima, Japan

<sup>2</sup>Institute of Laser Engineering, Osaka University, 2-6 Yamadaoka, Suita 565-0871, Osaka, Japan

<sup>3</sup>Department of Electrical and Electronic Engineering, Utsunomiya University, 350 Minemachi, Utsunomiya 321-8505, Tochigi, Japan

<sup>4</sup>Center for Material under Extreme Environment, Purdue University, 610 Purdue Mall, West Lafayette, Indiana 47907, USA



(Received 20 March 2023; accepted 23 May 2023; published 28 June 2023)

Optimal laser irradiation conditions for water-window (WW) x-ray emission (2.3–4.4 nm) from an Au plasma are investigated to develop a laboratory-scale WW x-ray source. A minimum Au target thickness of 1  $\mu\text{m}$  is obtained for a laser intensity of  $\sim 10^{13}$  W/cm<sup>2</sup> by observing the intensity drop in the WW spectra. Au targets produced by thermal evaporation are found to have a higher conversion efficiency than commercial foil targets for WW x-ray radiation. In addition, optimal laser spots for fixed laser energies (240 and 650 mJ) are found for an Au target  $\sim 1$  mm in front of the focal point, where suitable conditions for plasma temperature and plume volume coupling are achieved. The mechanism of the optimal target thickness and spot size can be well explained using a radiation hydrodynamic simulation code.

DOI: [10.1103/PhysRevE.107.065211](https://doi.org/10.1103/PhysRevE.107.065211)

### I. INTRODUCTION

Soft x-ray sources are highly anticipated for their potential use in diagnostic and manufacturing nanodevices. Research on their applications, such as x-ray lithography, x-ray holography, and x-ray microscopy, has been carried out since the last century [1,2]. In particular, soft x-rays in the so-called water-window (WW) region are important for biological research, as this wavelength range lies between the *K* absorption edges for carbon (4.4 nm) and oxygen (2.3 nm), exhibiting a high transmission contrast between atomic carbon and oxygen (water), which are the two main constituents of living organisms. Utilizing WW x rays allows x-ray microscopy imaging of relatively thick living organ samples without sample pre-treatments, such as dehydration and sectioning, in contrast to electron microscopy, which makes x-ray microscopy a favorable diagnostic tool for many circumstances [3,4]. With the improvement of zone plates and multilayer mirrors for focusing and collecting WW x rays [5–7], several practicable WW x-ray microscopy devices have been reported to date. Further research is underway to develop high-brightness WW x-ray sources, which are crucial for most laboratories to deploy WW x-ray microscopy for high-resolution images [8].

Several main schemes have been developed for producing WW x rays. Synchrotron radiation [9,10] and x-ray free-electron lasers [11] can generate strong WW x rays sufficient for resolutions of a few tens of nanometers, but these facilities are large and expensive, making them impractical for wide deployment. A discharge plasma [12] can produce stable,

sustainable WW x rays, although its relatively broad emission area results in low brightness [13]. Laser produced plasma (LPP) has also been considered suitable for WW x-ray sources [14–16]. Focused high-energy laser pulses allow intense WW emission to be confined to a small area in a plasma, giving a high-WW flux. It has been shown that a photon fluence of  $\sim 10^8$  photons/ $\mu\text{m}^2$  is required to obtain an x-ray microscopy image of protein with a spatial resolution under 50 nm and a signal-to-noise ratio over 5 [17]. However, the exposure time for a sample is also limited when considering practicability and the image blur caused by the Brownian motion of the particles [18]. Brilliance (brightness), which is defined as photons/(s $\times$ sr $\times$ mm<sup>2</sup> $\times$ 0.1% bandwidth (BW)), is often used to evaluate a WW x-ray source. An x-ray microscope using synchrotron radiation sources can achieve a brilliance of over  $10^{18}$  photons/(s $\times$ sr $\times$ mm<sup>2</sup> $\times$ 0.1% BW) [19]. In contrast, a permanent laser-plasma setup can reach a brilliance of only  $10^{12}$  photons/(s $\times$ sr $\times$ mm<sup>2</sup> $\times$ 0.1% BW) [20]. Therefore, enhancing conversion efficiency (CE) is the primary subject for LPP in developing a compact WW x-ray source.

In the LPP scheme, plasma is generated from laser-target interactions. The target material and shape strongly affect the x-ray emission yield. According to the quasi-Moseley law proposed by Ohashi *et al.* [21], x-ray spectra emitted from plasma of high-*Z* elements exhibit strong radiative transitions from the highly ionized ions, resulting in an unresolved transition array (UTA). In particular, laser-produced Au plasma produces UTA spectra with a peak in the WW region, providing abundant WW x rays, which are mainly attributed to  $n = 4-4$  and  $n = 4-5$  transitions in the highly charged Au ions. Moreover, John *et al.* [22] reported anomalous enhancement of WW emission from Au plasma under a N<sub>2</sub> gas atmosphere

\*namba@hiroshima-u.ac.jp

using a table-top Nd:Yttrium aluminum garnet (YAG) laser. To develop a practical WW x-ray source using laser-produced Au plasma, the target supply is one of the most important technical issues. Various target types for LPP, including foil [23,24], gas [25,26], liquid [27], foam [28], aerosol [29], and nanostructures [30,31], have been reported. For an Au target, foils can be employed as tape targets and irradiated at a 1-kHz repetition rate [32], making it possible to generate almost continuous WW emission.

Thinner Au targets are favorable for x-ray emission, as they not only tend to yield less debris, which is essential for extending an x-ray mirror's lifetime, but also significantly reduce the cost of the expensive Au target. Although various WW radiation conditions for Au thin foils have been investigated [24,33,34], no optimal thickness for WW radiation has been reported yet. The optimal focus condition of the incident laser beam also needs to be clarified, as the spot size drastically changes the laser intensity (fluence) as well as the size of the generated plasma plume. In an LPP, self-absorption (radiation trapping) occurs, where the x-rays emitted from the center of the hot dense plasma are reabsorbed by the peripheral plasma [35,36]. Thus, the effective x-ray yield that can be practically utilized is reduced considerably. The absorption coefficient for the plasma and the absorption length are strongly coupled with the fraction of self-absorption [37–39]. As the initial plasma condition is determined by laser ablation, optimizing the irradiation conditions is important for increasing the system CE.

In this work, WW UTA spectra emitted from Au plasma with different Au target thicknesses and laser focus conditions were investigated. The limit of Au layer thickness for a maximal WW emission with a laser intensity of  $10^{13}$  W/cm<sup>2</sup> was measured to be around 1  $\mu$ m. The optimal laser spot size at a fixed laser energy was also determined, where a larger plasma plume with a longer density scale length can emit more WW x rays than a tight focus condition. Also, Au targets manufactured by thermal physical vapor deposition show higher conversion efficiency to WW emission, based on which we deduce that the target nanostructure and thermal transfer mode of thin layers must make contributions.

## II. EXPERIMENTAL SETUP

A seeder-injected commercial Nd:YAG laser (wavelength: 1064 nm, repetition rate: 10 Hz, output energy: <1.2 J) was used in this work. The laser pulse energy was adjusted using infrared attenuator filters. The pulse duration was measured to be  $\tau_L = 6.2$  ns FWHM with a Gaussian energy distribution. To prevent reflection of the laser beam from the target surface or plasma back into the laser resonator, which would damage the optics, an optical isolator composed of a half-wave plate, a Faraday rotator, and a polarizer were installed in the beam-line [40]. However, due to nonlinear thermal effects in the polarizer under high laser intensity, the laser transverse mode and the beam pattern at the focal position were deformed. For single-shot measurements under a seeding laser mode, a customized mechanical shutter was installed in front of the Faraday rotator, picking up a single pulse while the laser itself operated in a stable 10-Hz mode. A thin glass plate was also placed in the beam pass to split 4% of the laser energy to a

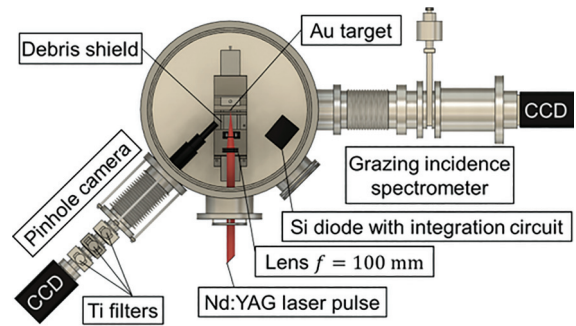


FIG. 1. Schematic of experimental setup for the laser-target and laser-plasma interaction vacuum chamber and four x-ray diagnostics apparatuses (GIS, pinhole camera, and Si PD).

calorimeter, monitoring the laser energy shot by shot during the experiments.

Two laser pulse energies,  $E_L = 650$  mJ and  $E_L = 240$  mJ, were used in this study, corresponding to on-target intensities of  $3.86 \times 10^{13}$  and  $1.43 \times 10^{13}$  W/cm<sup>2</sup>, respectively, for Gaussian spatiotemporal profiles. The laser beam was delivered into a vacuum chamber, focused onto Au targets with various thicknesses through a  $f = 100$  mm lens and a 0.2-mm-thick glass debris shield. The focused spot size was  $\phi_L = 15$   $\mu$ m FWHM. The lens and the target were mounted on multiaxis linear motorized stages which provided four degrees of freedom to the target and one degree to the lens, making it possible to achieve precise target-laser alignment. The vacuum chamber pressure was kept under  $\sim 10$  mPa using a dry pump and a turbomolecular pump during the experiments.

Three x-ray diagnostics apparatuses were installed in the chamber (shown in Fig. 1). A grazing incidence spectrometer (GIS) was attached to the chamber perpendicular to the laser incidence direction, comprising an Au coated toroidal mirror (size:  $50 \times 30$  mm<sup>2</sup>), a 2400 grooves/mm flatfield grating (Hitachi, size:  $50 \times 30$  mm<sup>2</sup>), an entrance slit width of 350  $\mu$ m, and a back illuminated x-ray charge-coupled device (X-CCD) camera (Andor iKon-M 934, pixel size:  $13 \times 13$   $\mu$ m<sup>2</sup>). Wavelength calibration in the WW region was conducted through hydrogen-like and helium-like line spectra from carbon plasmas [41]. Temporally integrated spectral emissions were measured through the GIS. A pinhole camera, consisting of a 25- $\mu$ m pinhole, an x-ray CCD, and Ti filters (0.5- and 1- $\mu$ m thicknesses), was installed at 45° to the target surface. The pinhole camera obtained spatial images of the time-integrated x-ray emission from the plasma. The magnification of the pinhole camera was measured to be  $M = 14$  with a resolution of 27  $\mu$ m. A Si photodiode (PD; 400- $\mu$ m pinhole, 1- $\mu$ m-thick Ti filter) connected to a charge amplifier was used to measure the integrated soft x-ray emission and was set 30 cm from the target surface at a 30° angle. The PD was triggered by another high-speed PD mounted on the top of the chamber, which received scattered laser light from the target as the trigger signal for the detector.

The Au targets were manufactured in two ways due to limitations of the fabrication process. For Au thicknesses of 10–300  $\mu$ m, commercial Au foils were cut into  $50 \times 12$  mm<sup>2</sup> squares and pasted on a 1-mm-thick glass plate using an acrylate copolymer. For Au thicknesses of 0.1–1.8  $\mu$ m, a thermal

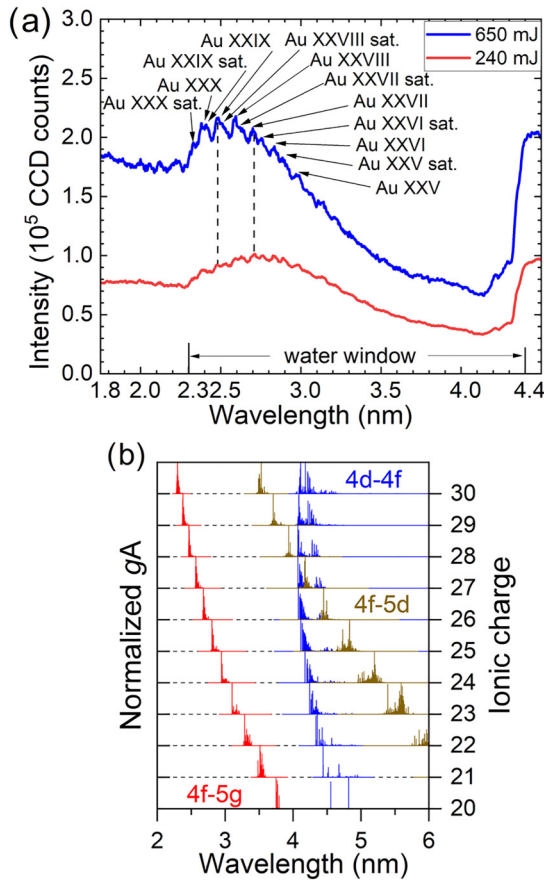


FIG. 2. (a) Spectra for 300- $\mu\text{m}$ -thick Au target produced by 650-mJ ( $3.86 \times 10^{13}$  W/cm $^2$ ) and 240-mJ ( $1.43 \times 10^{13}$  W/cm $^2$ ) laser pulses. Using the wavelength table [44], the charge states and surrounding satellite transitions were identified. The dashed lines indicate the peaks of the two spectra. (b) Weighted transition probabilities ( $gA$ ) contributing to WW emission, calculated by FAC.  $gA$  for 4d-4f, 4f-5d, and 4f-5g transitions from Au XXI to Au XXXI are shown.

physical vapor deposition apparatus was used to deposit Au vapor onto a glass plate. Experiment fluctuations due to the target roughness and thickness were considered. The surface conditions for the foil and deposition targets were different, which may have resulted in different laser-target interactions. For the thickness error of the deposition targets, theoretical errors during the deposition process were calculated [42] and are shown in Sec. III.

### III. RESULTS AND DISCUSSION

#### A. Fundamental aspect of Au laser plasmas

Soft x-ray spectra emitted from the Au plasma were measured with laser energies of 240 and 650 mJ under a tight focus condition (spot size = 15  $\mu\text{m}$ ). Typical GIS results for the Au spectra are shown in Fig. 2(a). The broadband spectra were produced by UTA emission from the countless energy levels in the highly ionized Au ions. The small peaks in the spectra can be attributed to UTAs from different charged Au ions and their satellite transitions. According to the transition possibility calculated by the Flexible Atomic Code (FAC) [43];

Fig. 2(b)],  $n = 4-4$  and  $n = 4-5$  transitions for Au ions mainly contribute to UTA emissions in the WW x-ray region. Emissions from 4f-5g tend to be of shorter wavelength as the ionization state of the dominant ions increases. This is in good agreement with the peak shift from 2.7 to 2.5 nm between the two Au spectra shown in Fig. 2(a). Due to the higher electron temperature generated by the higher laser energy, more Au ions with higher ionization states were produced, and the peak shifted to shorter wavelength. Soft x rays emitted from the Au plasma were observed through the pinhole camera with 0.5- and 1.0- $\mu\text{m}$  Ti filters, as shown in Fig. 3. Intense soft x rays were emitted from the center of the plasma, near the critical density region where the plasma was effectively heated by the Nd:YAG laser. The outer regions generated emissions from the subsequent expanded plasma, where the plasma was relatively cool and emitted longer-wavelength x rays. However, since the filter transmission is not perfectly matched with the WW region and the CCD sensor has inconstant quantum efficiency (QE) within this wavelength range, the following calibration procedure was employed to specify the x-ray wavelength observed by the pinhole camera (Fig. 4). The theoretical sensitivity of the pinhole camera was determined to be the product of the Ti filter transmission and the CCD quantum efficiency. Using the Au spectra obtained from Fig. 2(a), reference x-ray spectra for emissions observed by the pinhole camera were calculated, shown as red and blue lines in Fig. 4(a). According to the results, out-of-band x rays, shorter than 2.3 nm or longer than 4.4 nm, still contribute significantly to the pinhole image after filtering by the Ti. The attenuation rate was used to evaluate the difference between the emission intensities obtained using the two Ti filters. For the pinhole images, the attenuation rate was calculated by comparing the integration counts for the images, while the theoretical WW attenuation rate was calculated using the WW spectra from the two reference x-ray spectra. Although the GIS in this experiment was not calibrated, a comparison of the two attenuation rates was still valid in this case. The attenuation rate for the pinhole image was found to be 6 times larger than the WW attenuation rate in the reference x-ray spectra. This indicates that out-of-band x rays contribute significantly to the emission in the pinhole images.

The FWHM values for the soft x-ray emission size are shown in Fig. 3, illustrating a WW emission area smaller than 50  $\mu\text{m}$ , where highly charged Au ions were generated.

#### B. Optimal target thickness

The optimal Au thickness was investigated by evaluating x-ray emissions from plasmas produced from various Au targets for two different laser energies (650 and 240 mJ). All the plasmas were generated by tightly focused laser pulses with intensities of  $3.86 \times 10^{13}$  and  $1.43 \times 10^{13}$  W/cm $^2$ , respectively.

Figure 5(a) shows part of the Au spectra produced by deposition and foil targets for a laser energy of 650 mJ. The foil targets generated nearly constant spectral intensities. However, an enhancement is seen between the foil targets and the 1.8- $\mu\text{m}$ -thick deposition target. Line spectra from O and Si ions are also observed from the deposition targets. The spectral intensity gradually drops with decreasing deposition

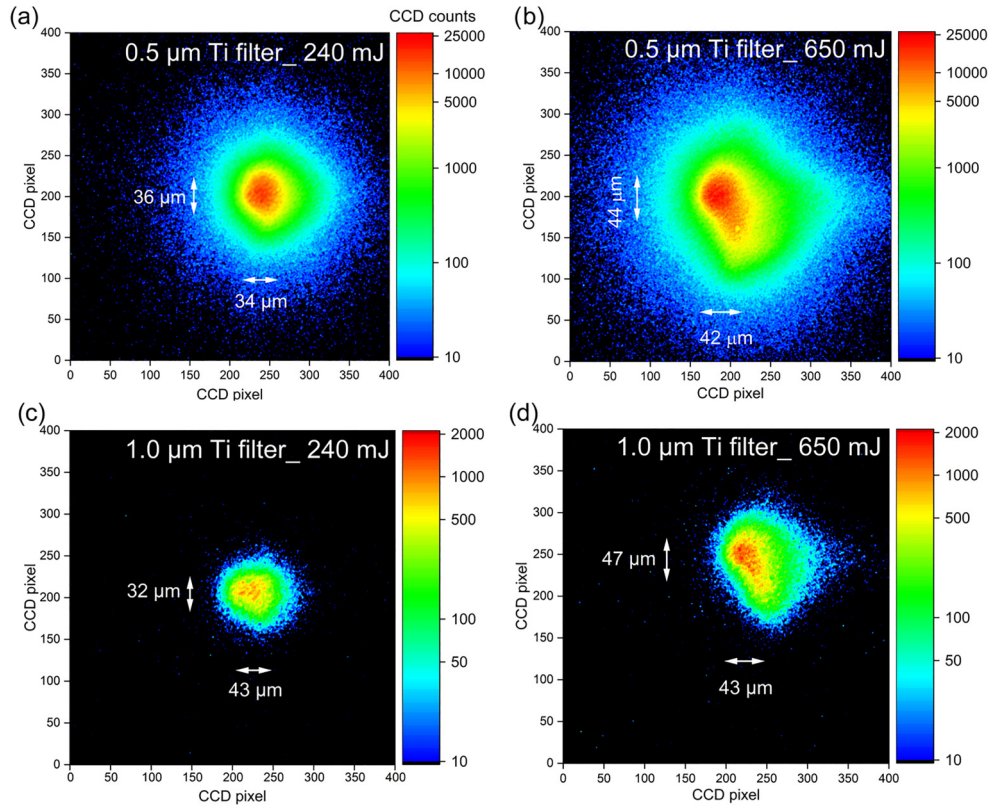


FIG. 3. Emissions from Au plasmas observed by the pinhole camera for different laser energies and Ti filters. A 30- $\mu\text{m}$ -thick Au foil was used as the target. (a) 0.5- $\mu\text{m}$ -thick Ti filter, 240 mJ ( $1.43 \times 10^{13}$  W/cm<sup>2</sup>), (b) 0.5- $\mu\text{m}$ -thick Ti filter, 650 mJ ( $3.86 \times 10^{13}$  W/cm<sup>2</sup>), (c) 1- $\mu\text{m}$ -thick Ti filter, 240 mJ, and (d) 1- $\mu\text{m}$ -thick Ti filter, 650 mJ. The solid arrows indicate the FWHM for the emission cross-section intensities in the horizontal and vertical directions.

target thickness until a constant UTA can no longer be observed.

The initial plasma was generated by laser ablation, where the laser has a characteristic heat conduction length. Depending on the Au layer thickness, this heat conduction length can lead to different thermal conduction processes in the initial period of ablation. For foil targets with thicknesses above 10

$\mu\text{m}$ , the heat conduction length is not comparable to the Au thickness, so three-dimensional (3D) hemispherical thermal transfer from the laser spot in the Au layer occurs. However, when the Au thickness is smaller than the laser spot radius, the thermal transfer direction changes from hemispherical to horizontal because of the thin Au layer. The large difference between the Au and glass thermal conductivities and heat capacities also contributes to this two-dimensional (2D) transfer mode [45–48]. Therefore, we considered the enhancement of the 1.8- $\mu\text{m}$ -thick Au spectrum to be caused by the different thermal transfer mode for the thick Au target, where laser interaction with the deposited Au atoms is more effective. The different microstructures of the two kinds of targets are also attributed to this effect. The results for the target surface observed by a microstructure scanning apparatus will be described later. The reason for the spectral intensity drop for thinner deposition targets can be explained by there being insufficient Au atoms in the irradiated region. As the Au layer is too thin, a considerable part of the laser pulse penetrates into the substrate glass plate (SiO<sub>2</sub>) and generates glass plasma. Thus, O and Si line spectra are observed for thinner deposition targets. The x-ray yields were evaluated by three approaches: integration of the CCD counts measured from the GIS spectra in the WW region, total CCD counts for the pinhole images (1.0- $\mu\text{m}$ -thick Ti filter), and the integrated Si photodiode signal from the charge amplifier (1.0- $\mu\text{m}$ -thick Ti filter), as shown in Fig. 5(b). Each data point in the plot is averaged from three experimental data values with a laser

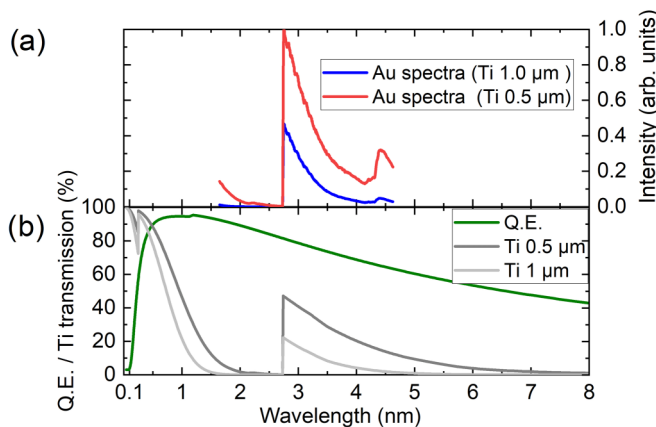


FIG. 4. (a) CCD QE and Ti foil filter transmission as a function of wavelength (green and gray lines). (b) The Au spectra (650-mJ laser energy) in Fig. 2(a) were used as reference spectra observed by the pinhole camera (blue and red lines).

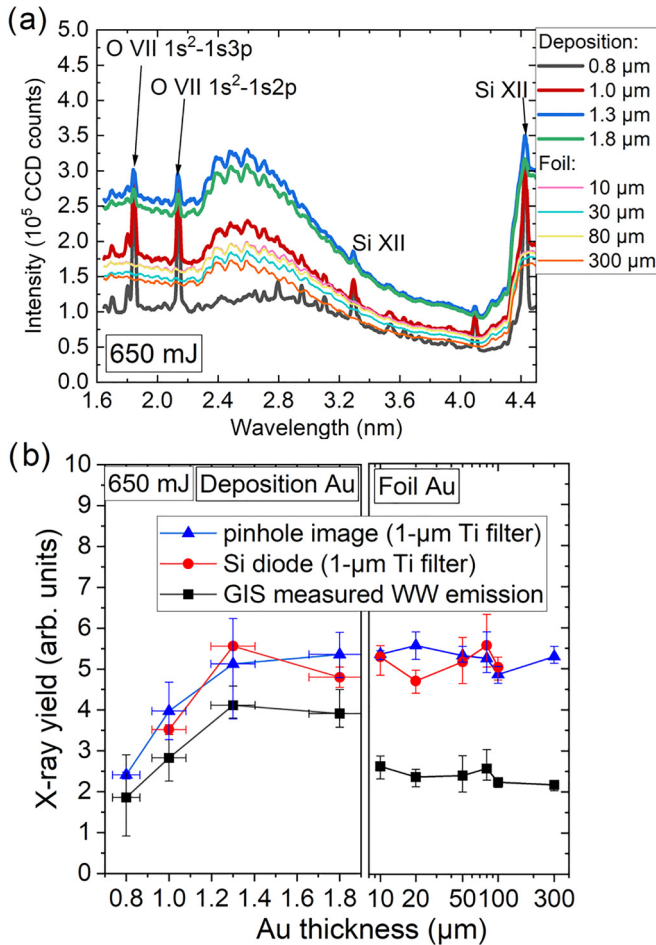


FIG. 5. (a) Au spectra for targets with various thicknesses produced by 650-mJ laser pulses ( $3.86 \times 10^{13}$  W/cm<sup>2</sup>). O and Si line spectra originating from the laser-glass interaction are observed for the deposition targets (0.8–1.8  $\mu$ m). The foil and deposition targets are shown as lines with different widths. (b) X-ray yield as a function of Au target thickness for 650-mJ laser energy, calculated by integrated pinhole image counts (blue), the integrated Si diode signal (red), and the WW region of the integrated GIS data (black). Note that the units for x-ray yield for the three results are largely irrelevant.

energy fluctuation within 10%. The vertical and horizontal error bars represent fluctuations of intensity and deposited Au thickness, respectively. All the detectors show nearly constant values from 300 to 10  $\mu$ m. The x-ray yield measured by the Si diode and pinhole camera did not show the same rise as the GIS data at 1.8 and 10  $\mu$ m. This is because out-of-band x rays, especially at wavelengths  $>4.3$  nm, significantly contributed to the x-ray yield for the former two detectors (see Fig. 4), while the GIS data included only the WW emission. The intensity rise observed by the GIS is caused by the different thermal conduction modes, as explained. A clear drop between 1.3 and 1.0  $\mu$ m for all three lines indicates that the thickness of the Au layer is no longer sufficient, although 70% of the x-ray yield could still be observed for targets with thicknesses less than 1.3  $\mu$ m.

An analysis of the Au surface microstructure was performed to elucidate the reason for the x-ray yield behavior. The surface microstructure of the commercial foil targets was

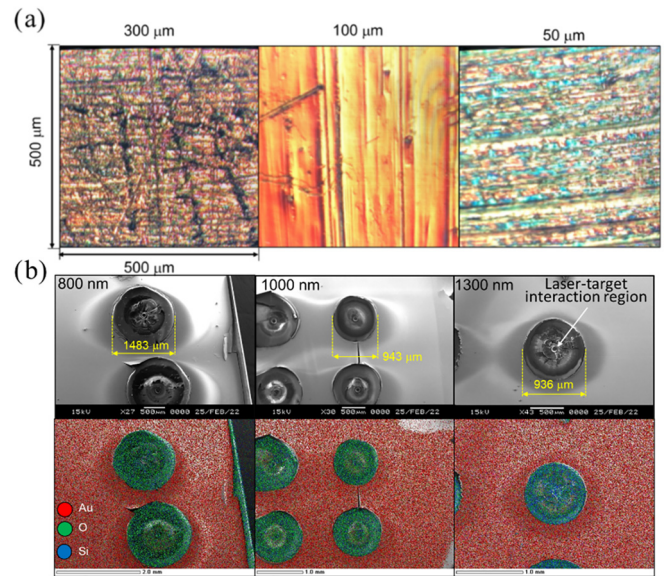


FIG. 6. (a) Au foil surfaces observed by optical microscope. (b) Top: SEM images of Au deposition target surfaces after irradiation with 650-mJ laser pulses. Bottom: EDS element analysis of the same area as in the top panel.

observed by an optical microscope, as shown in Fig. 6(a). Due to manufacturing limitations for these targets, the surface conditions show clear differences, which give different laser-target interactions and results for the fluctuations of the x-ray yield. Craters on the deposition targets appear in the top panel of Fig. 6(b), observed using a scanning electron microscopy (SEM). A dimple in the center of the crater was formed by the laser-target interaction, while the length marked in yellow indicates the melt zone for Au and glass, the area most affected by thermal heat conduction and subsequent ablation. The dimple on the glass plate for the 1.3- $\mu$ m-thick target illustrates that the minimum Au thickness (1.3  $\mu$ m) for sufficient WW x-ray emission is smaller than the characteristic depth of the dimple formed by laser ablation. Consequently, both normal level WW x rays and Si/O line spectra are observed from the plasma at 1.3- $\mu$ m target thickness. The surfaces were also analyzed to identify the elemental components by energy dispersive spectroscopy (EDS). The bottom panel in Fig. 6(b) shows that the deposited Au area was completely melted and ablated, and only Si and O elements were detected in the crater after 650-mJ laser irradiation.

For a laser energy of 240 mJ, thinner Au targets than in the 650-mJ case can be used to maximize the WW emission without ablating the SiO<sub>2</sub> layer, as shown in Fig. 7(a). In Fig. 7(b), the WW yield calculated from the GIS data for Au thicknesses ranging from 0.1 to 1.8  $\mu$ m is shown by the black squares and line. The WW yield rises as the Au thickness increases and then saturates at around 0.6  $\mu$ m. The x-ray yields obtained from the pinhole camera and Si diode show trends similar to that for the WW yield, indicating that the Au thickness limit is around 0.6  $\mu$ m for a laser energy of 240 mJ. To validate the results in Fig. 7, a 2D radiation-hydrodynamic simulation based on the STAR2D code [49] was carried out. The one-dimensional Lagrangian method combined with the

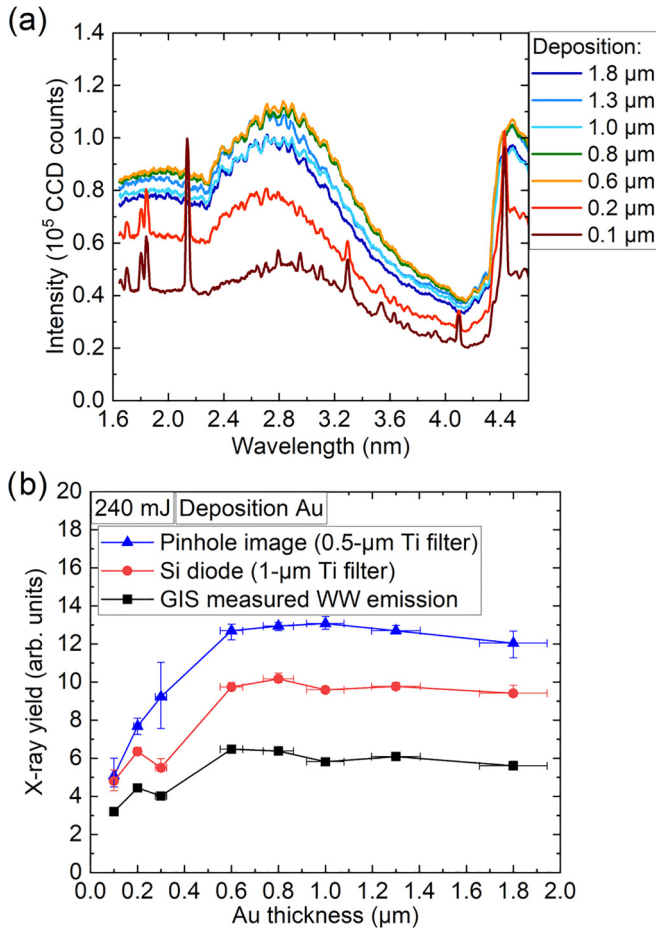


FIG. 7. (a) Au spectra for targets with different thicknesses produced by 240-mJ laser pulses. (b) X-ray yield as function of Au deposition target thickness for 240-mJ laser energy.

Eulerian method was used to calculate the plasma expansion process, and the vacuum space was set as a thin Au gas atmosphere for the calculation. Electrons and ions were treated in a one-fluid, two-temperature mode. SESAME EOS: The Los Alamos National Laboratory Equation of State Database (1995) table [50] and the opacity table calculated based on the screened hydrogenic averaged ion model [51] were adopted. The system was assumed to be axially symmetry in cylindrical coordinates ( $z, r$ ) and was unequally divided into cells, as shown in Fig. 8. The intersections of the grids were defined as the local isodensity point. A 2D simulation box with  $400(z) \times 200(r)$  grid cells is shown in the left panel of Fig. 8, where the Au target surface was set at  $z = 0 \mu\text{m}$  and the substrate  $\text{SiO}_2$  shown in yellow was set right behind it. During the actual calculations, the substrate layer was assumed to be the Au material with density equivalent to  $\text{SiO}_2$  to obtain stable solutions. The right panel in Fig. 8 shows a magnified view of the 1.2- $\mu\text{m}$ -thick Au target surface as an example. The red lines represent the cells in the Au-gas and Au-glass boundaries. The laser parameters were set to be the same as for the 240-mJ pulse case in the experiment.

To understand the physical dynamics and emission behavior when using targets with different thicknesses, the temporal evolution of the boundary between the Au and  $\text{SiO}_2$  was

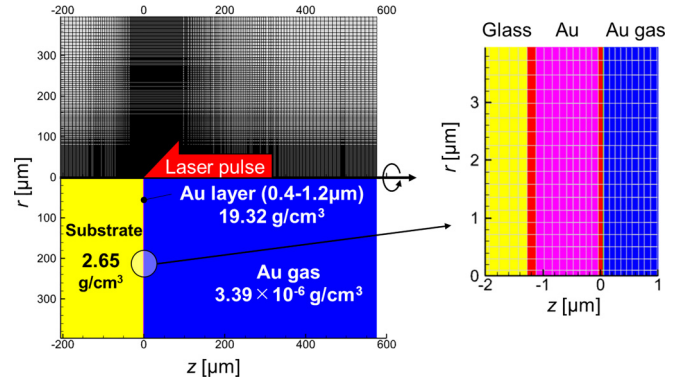


FIG. 8. Left: 2D simulation box shown in grid mode (top) and schematic mode (bottom). The laser incidence center axis is defined as the negative  $z$  direction, while  $r = 0$  is defined as the irradiation center. Right: Magnified view of grid cells around the target surface, showing glass (yellow), Au (pink), and gas (blue) layers. The red regions indicate the boundary between two layers, and  $z = 0$  is set as the surface of the Au layer.

traced as  $Z_{\text{bnd}}(r, t)$ . Figure 9 shows the average temporal evolution of the Au-glass boundary (top panel) when using different Au targets (thicknesses of 0.4, 0.6, 0.8, 1.0, and 1.2  $\mu\text{m}$ ), compared with the time evolution of the laser irradiation  $I_L(t)$  normalized by the peak intensity  $I_{L,\text{peak}}$  (bottom panel). The laser peak time was set to be  $t = 0$ .  $Z_{\text{bnd}}(r, t)$  ranging from  $r = 0 \mu\text{m}$  to  $r = 7.5 \mu\text{m}$  was averaged and defined as  $Z_{\text{bnd}}(t)$ , which is exactly the half-width at half maximum of the tightly focused laser spot. Note that the initial position of the boundary was defined as  $Z_{\text{bnd}} = 0$ . During the irradiation, the boundary moved initially in the negative  $z$  direction due to shock propagation driven by the laser irradiation and the ablation pressure. After the thin Au layer was fully ablated, the  $\text{SiO}_2$  layer was directly irradiated by the laser, and the boundary started to move in the positive  $z$  direction.

For Au thicknesses above 0.8  $\mu\text{m}$ , the laser peak intensity ( $t = 0 \text{ ns}$ ) passed before the Au layer was fully ablated, and

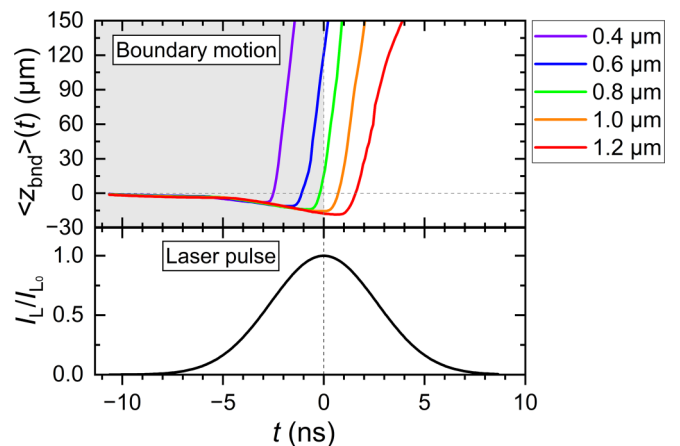


FIG. 9. The top panel shows the average temporal evolution of the Au-glass boundary during laser irradiation.  $Z_{\text{bnd}} = 0$  represents the initial  $z$  position of the boundary, as shown by the horizontal gray dashed line. The bottom panel shows the laser irradiation time evolution.

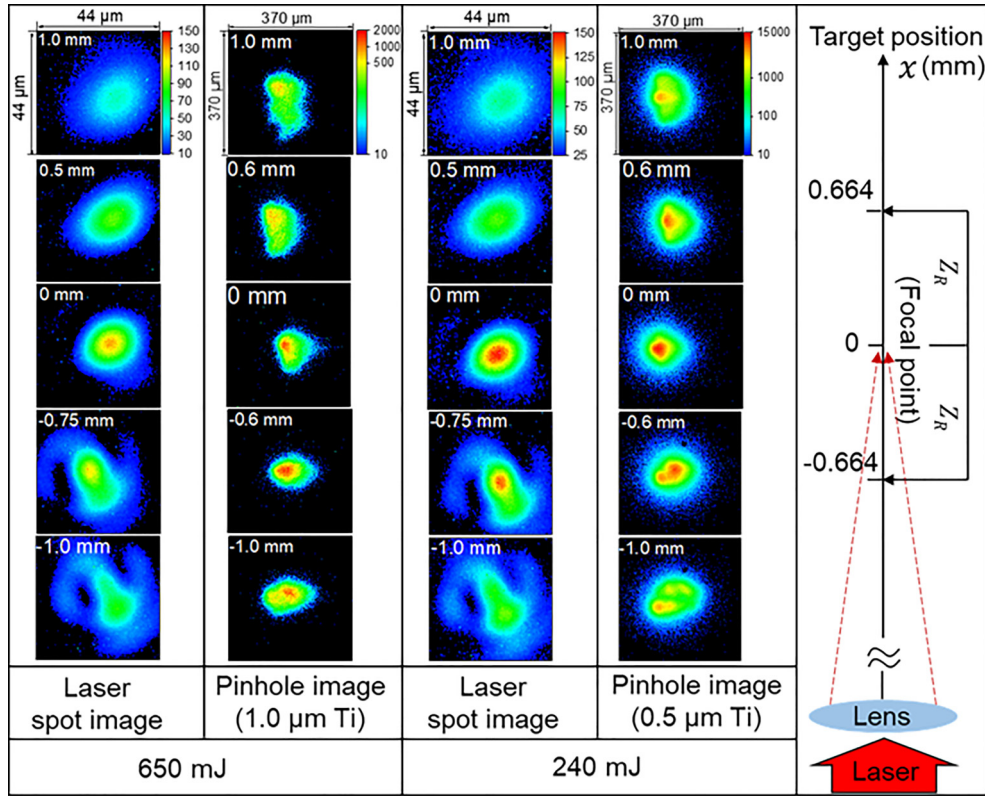


FIG. 10. Variations in laser spot images and pinhole images under different focus conditions. The target position was adjusted by moving the lens, and increasing focus distance corresponds to the positive direction. The  $x$  axis shows the focus condition for different target positions. In the right panel, the Rayleigh length  $Z_R$  and the focal point are denoted.

only the Au layer was ablated at the peak intensity. For target thicknesses below 0.6  $\mu\text{m}$ , the Au layer was fully ablated before the occurrence of the laser peak intensity, leading to high-intensity ablation of the glass layer, causing intense line spectra emissions from the irradiation center, while the outer Au plasma continued emitting x rays. Consequently, both line and UTA spectra could be observed in this case, which quantitatively explains the dependence of the WW emission on the Au thickness shown in Fig. 7(b).

### C. Optimal focus condition for higher x-ray yield

The focused laser spot sizes for different lens positions were measured for both 240- and 650-mJ laser energies using a 50- $\mu\text{m}$ -thick Au foil as a target. The target position was defined such that  $x = 0$  mm with the Au front surface precisely placed at the focal point of the focus lens. The spot size at the focal point was 15  $\mu\text{m}$ . Note that the target was fixed as a reference point during the entire measurement and the lens was moved back and forth with respect to the reference point, with the positive direction corresponding to a position with the target behind the focal point. Figure 10 shows focused laser spot images and pinhole images of the Au plasma (1.0- and 0.5- $\mu\text{m}$ -thick Ti filters) observed for various target positions. The laser spot images were measured by a complementary metal-oxide semiconductor camera set at  $x = 0$  mm, with the sensor surface perpendicular to the  $x$  axis. Within the Rayleigh length  $Z_R = 664$   $\mu\text{m}$ , almost all the laser spots had the same FWHM of 15  $\mu\text{m}$ , and the soft x-ray emission areas

were larger than the focused laser spot. As the spot shape started to blur as the target position was further changed, the laser spot and emission area became asymmetrical, resulting in a scattered x-ray distribution. Therefore, the spot size could no longer be calculated correctly. The laser spot shape remained similar when the target position moved in the positive direction, although the intensity gradually decreased. The energy distribution tended to be stable after the beam was focused on the focal point and irradiated the Au target behind. Compared with x-ray emission for  $x < 0$  mm, plasmas for  $x > 0$  mm were likely to radiate more centralized WW emission because of the more uniform Gaussian-distributed laser energy. WW emissions from plasma for various target positions were measured by the GIS, as shown in Figs. 11(a) and 11(b) for 650- and 240-mJ laser energies, respectively. An enhancement of the WW region is observed around  $x = -1.0$  and 1.0 mm for 650-mJ laser energy and  $x = -0.8$  and 0.6 mm for 240 mJ. Note that the GIS was not calibrated in terms of the toroidal mirror, grating, and CCD sensitivities. The peaks in the WW region are plotted as scatter lines. The spectral peaks shift to shorter wavelength as the target approaches  $x = 0$  mm, showing that Au ions with higher ionic charge are generated and dominate in the hot dense plasma. The x-ray yield trend can be explained as follows. The density scale length is strongly dependent on the spot size for plasma generated by nanosecond laser pulses. When the laser spot is moved away from the focal point, the density scale length becomes larger, providing a larger plasma plume. As the area for laser-plasma interaction increases, coupling between the

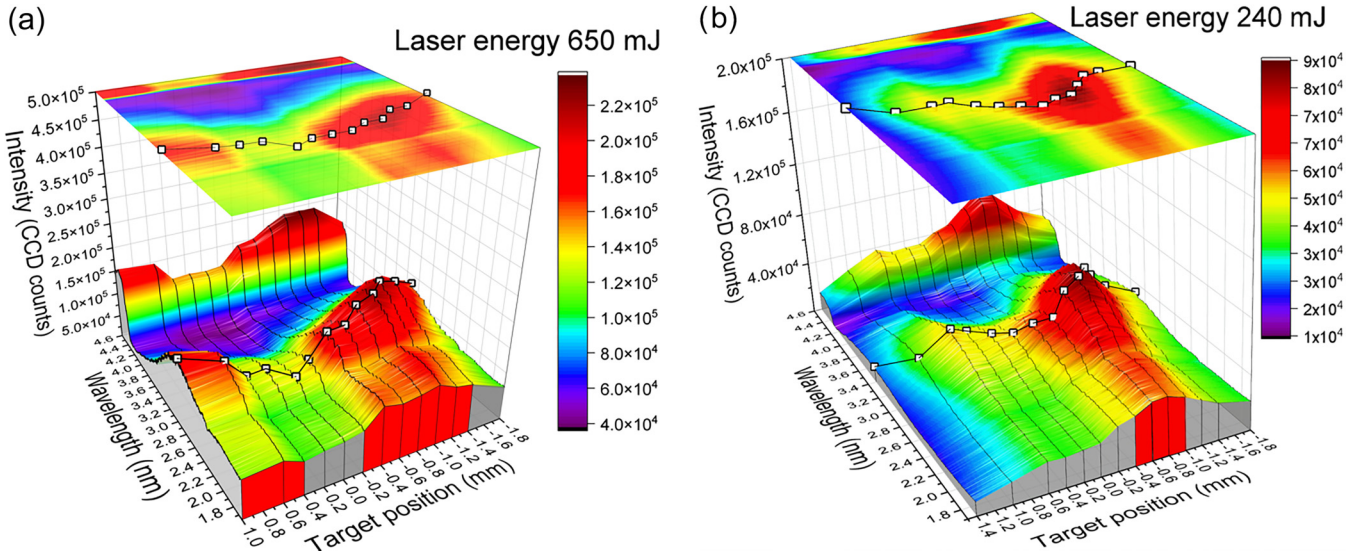


FIG. 11. GIS spectra as a function of target position for Au plasma produced by (a) 650-mJ and (b) 240-mJ laser irradiation. Two-dimensional contour plots are shown above each 3D plot. The scatter lines in (a) and (b) represent the peak WW wavelength of the corresponding 4f-5g transitions.

plasma temperature and plume volume produces a larger area favorable for WW emission at a slightly lower temperature [51,52]. Consequently, two WW emission peaks were observed on the two sides of the focal point position, with a slightly increased peak wavelength. Beyond the peak position, the insufficient laser intensity leads to a drop in both spectral intensity and peak wavelength, as shown in Fig. 11. Therefore, the optimal focus conditions providing a suitable laser irradiation intensity and Au plasma size for WW emission are  $x = -1.0$  mm for 650-mJ laser energy (spot size: 25  $\mu\text{m}$ , intensity:  $1.39 \times 10^{13}$  W/cm<sup>2</sup>) and  $x = -0.8$  mm for 240 mJ (spot size: 19  $\mu\text{m}$ , intensity:  $8.89 \times 10^{12}$  W/cm<sup>2</sup>). To further investigate the dependence of emission characteristics on laser focusing conditions, the STAR2D code was utilized to simulate the temporal evolution of the plasma for different irradiation spot sizes. The laser intensity and spot size on the target were varied for a fixed laser energy of  $E_L = 650$  mJ and pulse duration of  $\tau_L = 6.2$  ns. Table I shows the parameter settings

of the STAR2D simulation. The simulations were carried out for three spot sizes  $\phi_L$  (FWHM) and intensities  $I_{L,\text{peak}}$ :  $(\phi_L, I_{L,\text{peak}}) = (15 \mu\text{m}, 3.9 \times 10^{13} \text{ W/cm}^2)$ ,  $(33.5 \mu\text{m}, 0.77 \times 10^{13} \text{ W/cm}^2)$ , and  $(47.4 \mu\text{m}, 0.39 \times 10^{13} \text{ W/cm}^2)$ , corresponding to target positions of  $x = 0$  mm (focus position),  $-1.3$  mm, and  $-2.0$  mm, respectively. Figure 12 shows the spatial profile of electron temperature  $T_e$  and electron density  $n_e$  at the laser peak intensity. The electron temperature reaches over 300 eV, corresponding to the region where Au XXI-XXXI ions are generated. When the target is located at the focus position ( $x = 0$ ,  $\phi_L = 15 \mu\text{m}$ ,  $I_{L,\text{peak}} = 3.9 \times 10^{13}$  W/cm<sup>2</sup>), the plasma temperature exceeds 500 eV, which is far beyond the optimal electron temperature for WW emission ( $\sim 400$  eV). The width of the heated plasma is narrow due to the small spot size. Consequently, the peak wavelength of the emitted soft x-ray becomes shorter, and the emission region is small. In contrast, when the target is located far away from the focus position ( $x = -2.0$  mm,  $\phi_L = 47.4 \mu\text{m}$ ,  $I_{L,\text{peak}} =$

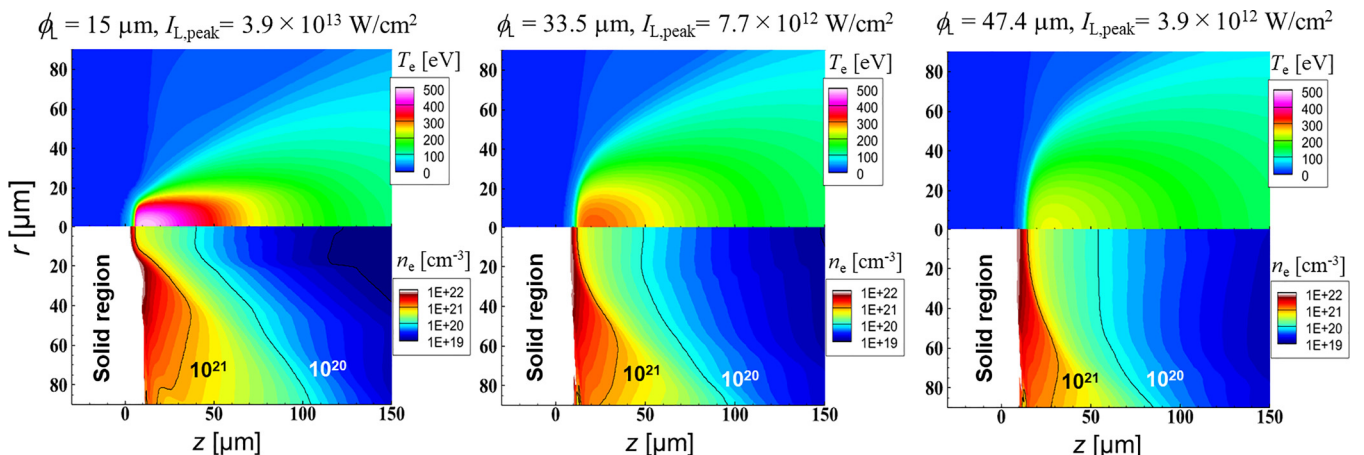


FIG. 12. Plasma profiles at the peak of laser irradiation intensity ( $t = 0$  ns).

TABLE I. Parameter settings for the STAR2D simulation.

Spot size $\phi_L$ ( $\mu\text{m}$ )	15	33.5	47.4
Peak intensity $I_{L,\text{peak}}$ ( $10^{13}$ W/cm <sup>3</sup> )	3.9	0.77	0.39
Target position (mm)	0	-1.3	-2.0

$0.39 \times 10^{13}$  W/cm<sup>2</sup>), the laser intensity is too low to produce plasma with a suitable temperature for WW emission, even though the plasma heated by the laser is much wider than that for the small spot size. With the present laser conditions ( $E_L = 650$  mJ and  $\tau_L = 6.2$  ns), the optimal laser irradiation condition forming a suitable temperature  $T_e$  and heated plasma volume for WW emission is  $\phi_L = 33.5$   $\mu\text{m}$ , corresponding to a target position of  $x = -1.3$  mm. These results show that the WW emission trends from the simulation are in good agreement with the experimental results.

#### IV. CONCLUSION

In this work, the optimal target thickness and laser irradiation conditions for a WW x-ray source based on laser-produced Au plasma were studied. The UTA spectra, which were mainly attributed to  $4f$ - $5g$  transitions for  $\text{Au}^{20+}$ - $\text{Au}^{30+}$  ions, were measured and evaluated to determine the emission behavior. The Au thickness limits for 650 mJ ( $3.86 \times 10^{13}$  W/cm<sup>2</sup>) and 240 mJ ( $1.43 \times 10^{13}$  W/cm<sup>2</sup>) were determined to be 1.3 and 0.6  $\mu\text{m}$ , respectively, below which the layer is too thin and can be fully ablated before the pulse peak reaches the surface, according to simulation results from STAR2D. Larger plasma plumes with longer density scale lengths and appropriate laser intensities were found to be favorable for WW emission when the target was positioned 1.0 and 0.8 mm in front of the focal point for laser energies of 650 and 240 mJ, respectively. The simulation results showed the same WW emission trend as the experimental results. Overall, these optimizations can lead to an LPP scheme with higher CE as a WW radiation source.

- [1] J. Kirz, C. Jacobsen, and M. Howells, Soft x-ray microscopes and their biological applications, *Q. Rev. Biophys.* **28**, 33 (1995).
- [2] E. W. Becker, W. Ehrfeld, P. Hagmann, A. Maner, and D. Münchmeyer, Fabrication of microstructures with high aspect ratios and great structural heights by synchrotron radiation lithography, galvanofarming, and plastic moulding (LIGA process), *Microelectron. Eng.* **4**, 35 (1986).
- [3] A. Weiner, S. Kapishnikov, E. Shimoni, S. Cordes, P. Guttmann, G. Schneider, and M. Elbaum, Vitriification of thick samples for soft x-ray cryo-tomography by high pressure freezing, *J. Struct. Biol.* **181**, 77 (2013).
- [4] C. Nave, A comparison of absorption and phase contrast for x-ray imaging of biological cells, *J. Synchrotron Radiat.* **25**, 1490 (2018).
- [5] M. Ishino, O. Yoda, and M. Koike, Development of multilayer mirrors for use in the wavelength region of 4 nm, Report No.: JAERI-Research 2005-019 (2005), p. 13.
- [6] W. Chao, B. D. Harteneck, J. A. Liddle, E. H. Anderson, and D. T. Attwood, Soft X-ray microscopy at a spatial resolution better than 15 nm, *Nature (London)* **435**, 1210 (2005).
- [7] F. Eriksson, G. A. Johansson, H. M. Hertz, E. M. Gullikson, U. Kreissig, and J. Birch, 14.5% near-normal incidence reflectance of Cr/Sc x-ray multilayer mirrors for the water window, *Opt. Lett.* **28**, 2494 (2003).
- [8] D. Sayre, J. Kirz, R. Feder, D. M. Kim, and E. Spiller, Potential operating region for ultrasoft x-ray microscopy of biological materials, *Science* **196**, 1339 (1977).
- [9] C. Jacobsen and J. Kirz, X-ray microscopy with synchrotron radiation, *Nat. Struct. Biol.* **5**, 650 (1998).
- [10] E. Pereiro, J. Nicolás, S. Ferrer, and M. R. Howells, A soft x-ray beamline for transmission x-ray microscopy at ALBA, *J. Synchrotron Radiat.* **16**, 505 (2009).
- [11] W. Ackermann *et al.*, Operation of a free-electron laser from the extreme ultraviolet to the water window, *Nat. Photon.* **1**, 336 (2007).
- [12] T. Parkman, M. Nevrkla, A. Jančárek, J. Turňová, D. Pánek, and M. Vrbová, Table-top water-window microscope using a capillary discharge plasma source with spatial resolution 75 nm, *Appl. Sci.* **10**, 6373 (2020).
- [13] M. Kördel, A. Dehlinger, C. Seim, U. Vogt, E. Fogelqvist, J. A. Sellberg, H. Stiel, and H. M. Hertz, Laboratory water-window x-ray microscopy, *Opt. Soc. Am.* **7**, 658 (2020).
- [14] M. Kishimoto, M. Kado, M. Ishino, S. Tamotsu, K. Yasuda, and K. Shinohara, Development of single shot soft x-ray contact microscopy system for nano-scale dynamics measurement of living biological specimen, in *Laser-Driven Relativistic Plasmas Applied to Science, Energy, Industry, and Medicine: The 3rd International Symposium*, AIP Conf. Proc. No. 1465 (AIP, Melville, NY, 2012), p. 43.
- [15] A. G. Michette, I. C. Turcu, M. S. Schulz, M. T. Browne, G. R. Morrison, P. Fluck, C. J. Buckley, and G. F. Foster, Scanning x-ray microscopy using a laser-plasma source, *Rev. Sci. Instrum.* **64**, 1478 (1993).
- [16] C. John, M. Kishimoto, Y. Matsumoto, T. Morishita, T. Higashiguchi, T. Endo, A. Sunahara, T. Johzaki, and S. Namba, Observation of water-window soft x-ray emission from laser-produced Au plasma under optically thin condition, *High Energy Density Phys.* **37**, 100845 (2020).
- [17] D. Sayre, J. Kirz, R. Feder, D. M. Kim, and E. Spiller, Transmission microscopy of unmodified biological materials. Comparative radiation dosages with electrons and ultrasoft x-ray photons, *Ultramicroscopy* **2**, 337 (1976).
- [18] A. Ito, T. Inoue, M. Kado, T. Ohigashi, S. Tone, and K. Shinohara, Biomedical application of soft x-ray microscopy with special reference to spectromicroscopy, *Acta Phys. Pol. A* **129**, 260 (2016).
- [19] Machine Information, <https://als.lbl.gov/machine-information/>.
- [20] D. H. Martz, M. Selin, O. von Hofsten, E. Fogelqvist, A. Holmberg, U. Vogt, H. Legall, G. Blobel, C. Seim, H. Stiel, and H. M. Hertz, High average brightness water window source for short-exposure cryomicroscopy, *Opt. Lett.* **37**, 4425 (2012).

- [21] H. Ohashi, T. Higashiguchi, Y. Suzuki, G. Arai, Y. Otani, T. Yatagai, B. Li, P. Dunne, G. O'Sullivan, W. Jiang, A. Endo, H. A. Sakaue, D. Kato, I. Murakami, N. Tamura, S. Sudo, F. Koike, and C. Suzuki, Quasi-Moseley's law for strong narrow bandwidth soft x-ray sources containing higher charge-state ions, *Appl. Phys. Lett.* **104**, 234107 (2014).
- [22] C. John, M. Kishimoto, T. Johzaki, T. Higashiguchi, N. Kakunaka, Y. Matsumoto, N. Hasegawa, M. Nishikino, T. Ejima, A. Sunahara, T. Endo, and S. Namba, Enhancement of water-window soft x-ray emission from laser-produced Au plasma under low-pressure nitrogen atmosphere, *Opt. Lett.* **44**, 1439 (2019).
- [23] B. J. MacGowan, S. Maxon, P. L. Hagelstein, C. J. Keane, R. A. London, D. L. Matthews, M. D. Rosen, J. H. Scofield, and D. A. Whelan, Demonstration of Soft X-Ray Amplification in Nickel-Like Ions, *Phys. Rev. Lett.* **59**, 2157 (1987).
- [24] J. S. Davis, R. P. Drake, M. Fraenkel, Y. Frank, P. A. Keiter, S. R. Klein, E. Raicher, D. Shvarts, and M. R. Trantham, Soft X-ray emission from laser-irradiated gold foils, *Phys. Plasma* **25**, 073304 (2018).
- [25] P. W. Wachulak, Recent advancements in the "water-window" microscopy with laser-plasma SXR source based on a double stream gas-puff target, *Opto-Electron. Rev.* **24**, 144 (2016).
- [26] G. J. Stein, P. D. Keathley, P. Krogen, H. Liang, J. P. Siqueira, C.-L. Chang, C.-J. Lai, K.-H. Hong, G. M. Laurent, and F. X. Kärtner, Water-window soft x-ray high-harmonic generation up to the nitrogen K-edge driven by a kHz, 2.1  $\mu\text{m}$  OPCPA source, *J. Phys. B* **49**, 155601 (2016).
- [27] G. A. Johansson, A. Holmberg, H. M. Hertz, and M. Berglund, Design and performance of a laser-plasma-based compact soft x-ray microscope, *Rev. Sci. Instrum.* **73**, 1193 (2002).
- [28] Y. Dong, L. Zhang, J. Yang, and W. Shang, Detailed energy distributions in laser-produced plasmas of solid gold and foam gold planar targets, *Phys. Plasma* **20**, 1 (2013).
- [29] Ł. Wgrzyński, A. Bartnik, P. Wachulak, T. Fok, and H. Fiedorowicz, Laser-produced plasma soft x-ray source based on an aerosol target, *Phys. Plasma* **27** (2020).
- [30] Y. Shou, D. Kong, P. Wang, Z. Mei, Z. Cao, Z. Pan, Y. Li, S. Xu, G. Qi, S. Chen, J. Zhao, Y. Zhao, C. Fu, W. Luo, G. Zhang, X. Yan, and W. Ma, High-efficiency water-window x-ray generation from nanowire array targets irradiated with femtosecond laser pulses, *Opt. Express* **29**, 5427 (2021).
- [31] H. Tanaka, K. Akinaga, A. Takahashi, and T. Okada, Development of a target for laser-produced plasma EUV light source using Sn nano-particles, *Appl. Phys. A* **79**, 1493 (2004).
- [32] A. Koc, C. Hauf, M. Woerner, L. V. Grafenstein, D. Ueberschaer, M. Bock, U. Griebner, and T. Elsaesser, High-flux table-top hard x-ray source driven by femtosecond mid-infrared pulses at a 1 kHz repetition rate, in *Proceedings of 2021 Conference on Lasers and Electro-Optics, CLEO 2021* (Optical Society of America, Washington, DC, 2021), p. 210.
- [33] M. Ishino, M. Kado, M. Nishikino, K. Shinohara, S. Tamotsu, K. Yasuda, N. Hasegawa, M. Kishimoto, T. Ohba, and T. Kawachi, Observations of the intense soft x-ray emissions from ultrathin Au films irradiated with high contrast laser pulses, *Proc. SPIE* **7589**, 75891 (2010).
- [34] S. L. Pape, L. Divol, A. Macphee, J. McNaney, M. Hohenberger, D. Froula, V. Glebov, O. L. Landen, C. Stoeckl, E. Dewald, S. Khan, C. Yeaman, P. Michel, M. Schneider, J. Knauer, J. Kilkenny, and A. J. Mackinnon, Optimization of high energy x ray production through laser plasma interaction, *High Energy Density Phys.* **31**, 13 (2019).
- [35] H. Hara, H. Kawasaki, T. Tamura, T. Hatano, T. Ejima, W. Jiang, H. Ohashi, S. Namba, A. Sunahara, A. Sasaki, M. Nishikino, G. O'Sullivan, and T. Higashiguchi, Emission of water-window soft x-rays under optically thin conditions using low-density foam targets, *Opt. Lett.* **43**, 3750 (2018).
- [36] S. Fujioka, H. Nishimura, K. Nishihara, A. Sasaki, A. Sunahara, T. Okuno, N. Ueda, T. Ando, Y. Tao, Y. Shimada, K. Hashimoto, M. Yamaura, K. Shigemori, M. Nakai, K. Nagai, T. Norimatsu, T. Nishikawa, and N. Miyanaga, Opacity Effect on Extreme Ultraviolet Radiation from Laser-Produced Tin Plasmas, *Phys. Rev. Lett.* **95**, 235004 (2005).
- [37] J. J. Hou, L. Zhang, Y. Zhao, X. Yan, W. Ma, L. Dong, W. Yin, L. Xiao, and S. Jia, Laser-induced plasma characterization through self-absorption quantification, *J. Quant. Spectrosc. Radiat. Transfer* **213**, 143 (2018).
- [38] A. M. E. Sherbini, T. M. E. Sherbini, H. Hegazy, G. Cristoforetti, S. Legnaioli, V. Palleschi, L. Pardini, A. Salvetti, and E. Tognoni, Evaluation of self-absorption coefficients of aluminum emission lines in laser-induced breakdown spectroscopy measurements, *Spectrochim. Acta Part B* **60**, 1573 (2005).
- [39] C. Aragón, J. Bengoechea, and J. A. Aguilera, Influence of the optical depth on spectral line emission from laser-induced plasmas, *Spectrochim. Acta Part B* **56**, 619 (2001).
- [40] B. E. A. Saleh and M. C. Teich, in *Fundamentals of Photonics*, edited by J. W. Goodman, *Fundamentals of Photonics* (Wiley, New York, 1991).
- [41] A. Kramida, Y. Ralchenko, J. Reader, and NIST ASD Team, *NIST Atomic Spectra Database* (version 5.10) [Online] (National Institute of Standards and Technology, Gaithersburg, MD, 2022).
- [42] L. Holland and J. Greenspan, Vacuum deposition of thin films, *J. Electrochem. Soc.* **104**, 116C (1957).
- [43] M. F. Gu, The flexible atomic code, *Can. J. Phys.* **86**, 675 (2008).
- [44] B. Li, T. Higashiguchi, T. Otsuka, N. Yugami, P. Dunne, D. Kilbane, E. Sokell, and G. O'Sullivan, Analysis of laser produced plasmas of gold in the 1-7 nm region, *J. Phys. B: At. Mol. Opt. Phys.* **47**, 075001 (2014).
- [45] V. M. Shugaev, M. He, Y. Levy, A. Mazzi, A. Miotello, N. M. Bulgakova, and V. L. Zhigilei, Laser-induced thermal processes: Heat transfer, generation of stresses, melting and solidification, vaporization, and phase explosion, in *Handbook of Laser Micro- and Nano-Engineering*, edited by K. Sugioka (Springer, Cham, 2020), pp. 1–81.
- [46] H. Daido and A. Sasaki, Material Property and Simulation Methods Applicable to Laser Produced Plasmas in the New Density and Temperature Region, *J. Plasma Fusion Res.* **89**, 403 (2013).
- [47] B. Rethfeld, D. S. Ivanov, M. E. Garcia, and S. I. Anisimov, Modelling ultrafast laser ablation, *J. Phys. D* **50**, 193001 (2017).
- [48] A. Sunahara, Initial process of laser-plasma interaction in the extreme ultra-violet light source and the inertial confinement fusion plasmas, *J. Plasma Fusion Res.* **89**, 416 (2013).
- [49] S. P. Lyon and J. D. Johnson, SESAME: The Los Alamos National Laboratory Equation of State Database Contents (1992), [www.lanl.gov](http://www.lanl.gov).

- [50] D. Saltzmann, *Atomic Physics in Hot Plasmas* (Oxford University Press, Oxford, 1998).
- [51] R. Kodama, T. Mochizuki, K. A. Tanaka, and C. Yamanaka, Enhancement of keV x-ray emission in laser-produced plasmas by a weak prepulse laser, *Appl. Phys. Lett.* **50**, 720 (1987).
- [52] R. J. Gray, R. Wilson, M. King, S. D. Williamson, R. J. Dance, C. Armstrong, C. Brabetz, F. Wagner, B. Zielbauer, V. Bagnoud, D. Neely, and P. McKenna, Enhanced laser-energy coupling to dense plasmas driven by recirculating electron currents, *New J. Phys.* **20**, 033021 (2018).